

Loop-cluster simulation of the zero- and one-hole sectors of the t - J model on the honeycomb lattice

F.-J. Jiang,^{*} F. Kämpfer,[†] M. Nyfeler,[‡] and U.-J. Wiese[§]

Center for Research and Education in Fundamental Physics, Institute for Theoretical Physics, Bern University, Sidlerstrasse 5, CH-3012 Bern, Switzerland

(Received 25 July 2008; revised manuscript received 21 October 2008; published 5 December 2008)

Inspired by the unhydrated variant of the superconducting material $\text{Na}_x\text{CoO}_2 \cdot y\text{H}_2\text{O}$ at $x = \frac{1}{3}$, we study the t - J model on a honeycomb lattice by using an efficient loop-cluster algorithm. The low-energy physics of the undoped system and of the single-hole sector is described by a systematic low-energy effective field theory. The staggered magnetization per spin $\tilde{M}_s = 0.2688(3)$, the spin stiffness $\rho_s = 0.102(2)J$, the spin-wave velocity $c = 1.297(16)Ja$, and the kinetic mass M' of a hole are obtained by fitting the numerical Monte Carlo data to the effective field theory predictions.

DOI: [10.1103/PhysRevB.78.214406](https://doi.org/10.1103/PhysRevB.78.214406)

PACS number(s): 72.30.Fe, 75.10.Jm, 75.40.Mg, 75.50.Ee

I. INTRODUCTION

Since the discovery of high-temperature superconductivity in cuprate materials,¹ the Hubbard and t - J models have been of central importance in strongly correlated electron systems. However, due to their strong coupling, a systematic analytic treatment of these models is currently not available. Similarly, a severe sign problem away from half filling prevents us from understanding these systems quantitatively by reliable Monte Carlo calculations. Despite these difficulties, much effort has been devoted to understanding the properties of t - J -type models on the square lattice. Although some controversial results have been obtained, various studies including exact diagonalization,^{2,3} series expansion,⁴ and Monte Carlo simulations^{5,6} enable us to understand the hole dynamics quantitatively, at least to some extent. In particular, these studies all obtained minima of the single-hole dispersion relation at lattice momenta $(\pm \frac{\pi}{2a}, \pm \frac{\pi}{2a})$ in the Brillouin zone of the square lattice which is in agreement with experimental results.⁷⁻⁹

A reliable and order-by-order exact way to investigate the low-energy physics of lightly doped antiferromagnets is provided by a systematic low-energy effective field theory. The physics of the undoped systems is quantitatively described by magnon chiral perturbation theory,¹⁰⁻¹⁴ while the interactions of magnons and holes are described by a low-energy effective theory for hole-doped antiferromagnets.^{15,16} Predictions of the effective theory only depend on a small number of low-energy constants which can be determined from either experiments or Monte Carlo data. Thus, the use of low-energy effective theories together with reliable Monte Carlo simulations provides an unbiased approach to studying the low-energy physics of these systems. In particular, using the loop-cluster algorithm,¹⁷ the low-energy parameters of the spin-1/2 Heisenberg model have been determined with very high precision.^{18,19} Indeed, thanks to the combination of very efficient Monte Carlo simulations with the systematic low-energy effective field theory, undoped antiferromagnets on the square-lattice such as La_2CuO_4 and $\text{Sr}_2\text{CuO}_2\text{Cl}_2$ are among the quantitatively best-understood condensed matter systems.

In addition to the cuprates, another superconducting material, $\text{Na}_x\text{CoO}_2 \cdot y\text{H}_2\text{O}$, has drawn a lot of attention both

theoretically and experimentally. Unfortunately, due to the fact that the underlying lattice geometry of the spin-1/2 cobalt sites in these materials is triangular—which leads to strong geometric frustration—a first-principles Monte Carlo study is impossible in practice. Nevertheless, the spin- and charge-ordering tendencies observed and studied in Refs. 20–22 may suggest that at filling $x = \frac{1}{3}$, the unhydrated parent compound Na_xCoO_2 can be described by the t - J model on a half-filled honeycomb lattice which allows one to simulate the system efficiently with the loop-cluster algorithm.

Another system on the honeycomb lattice that has been investigated with great vigor is graphene—a single sheet of graphite (see Ref. 23 for a detailed review). As a consequence of the geometry of the honeycomb lattice, the low-energy excitations of graphene are massless Dirac fermions. If some variant of graphene would exist at stronger coupling, one would eventually expect a phase transition separating graphene's unbroken phase from a strong-coupling antiferromagnetic phase in which the $\text{SU}(2)_s$ spin symmetry is spontaneously broken to $\text{U}(1)_s$. The low-energy effective theory of the unbroken phase and of the critical point has been constructed in Ref. 24.

Motivated by possible applications to Na_xCoO_2 , we investigate the spin-1/2 Heisenberg model as well as the t - J model on the honeycomb lattice by using the quantum Monte Carlo method. Just as in the square lattice case, the long-distance physics of these models is described quantitatively by a systematic low-energy effective field theory. At low energies, the Heisenberg model on a bipartite lattice is described by magnon chiral perturbation theory, and accordingly, the t - J model is described by a low-energy effective field theory for magnons and holes. Based on the same method that has been used in the square lattice case, we have constructed the leading-order terms in the action of a systematic low-energy effective field theory for magnons and holes on the honeycomb lattice. In this paper, we determine the corresponding leading-order low-energy constants, namely, the staggered magnetization per spin \tilde{M}_s , which was also obtained in Ref. 25, the spin stiffness ρ_s , the spin-wave velocity c , and the kinetic mass M' of a doped hole by fitting the Monte Carlo data to the effective field theory predictions. We also investigate the bandwidth and the quasiparticle weight of a single

hole on the honeycomb lattice, which have already been studied in Ref. 26.

The rest of this paper is organized as follows. In Sec. II, we introduce the relevant microscopic models as well as corresponding observables. Section III reviews the low-energy effective theory for magnons, and Sec. IV is devoted to the Monte Carlo determination of the corresponding low-energy parameters. The single-hole physics is investigated in Sec. V, and the effective theory for holes and magnons is discussed in Sec. VI, while Sec. VII contains our conclusions. The basics of the numerical method to simulate the one-hole sector are described in the Appendix.

II. MICROSCOPIC MODELS AND CORRESPONDING OBSERVABLES

In this section we introduce the Hamiltonians of the microscopic t - J model and the Heisenberg model as well as some relevant observables. The t - J model is defined by the Hamiltonian operator

$$H = P \left\{ -t \sum_{\langle xy \rangle} (c_x^\dagger c_y + c_y^\dagger c_x) + J \sum_{\langle xy \rangle} \vec{S}_x \cdot \vec{S}_y \right\} P. \quad (1)$$

Here c_x^\dagger and c_x are fermion creation and annihilation operators at a site x with

$$c_x = \begin{pmatrix} c_{x\uparrow} \\ c_{x\downarrow} \end{pmatrix}, \quad (2)$$

whose components obey standard anticommutation relations. In terms of the Pauli matrices $\vec{\sigma}$ the local spin operator at a site x is given by

$$\vec{S}_x = c_x^\dagger \frac{\vec{\sigma}}{2} c_x. \quad (3)$$

The projection operator P restricts the Hilbert space by eliminating doubly occupied sites. Hence the t - J model allows empty or singly occupied sites only. The hopping of fermions is controlled by the parameter t , while $J > 0$ is the antiferromagnetic exchange coupling between neighboring spins. At half filling, the t - J model reduces to the Heisenberg model with the Hamiltonian

$$H = J \sum_{\langle xy \rangle} \vec{S}_x \cdot \vec{S}_y. \quad (4)$$

The honeycomb lattice with periodic spatial boundary conditions implemented in our simulations is depicted in Fig. 1. The dashed rectangle in Fig. 1, which contains four spins, is the elementary cell for building a periodic honeycomb lattice covering a rectangular area. For instance, the honeycomb lattice shown in Fig. 1 contains 3×3 elementary cells. The lattice spacing a is the distance between two neighboring sites. The honeycomb lattice is not a Bravais lattice. Instead it consists of two triangular Bravais sublattices A and B (depicted by solid and open circles in Fig. 1). As a consequence, the momentum space of the honeycomb lattice is a doubly covered Brillouin zone of the two triangular sublattices (depicted in Fig. 2).

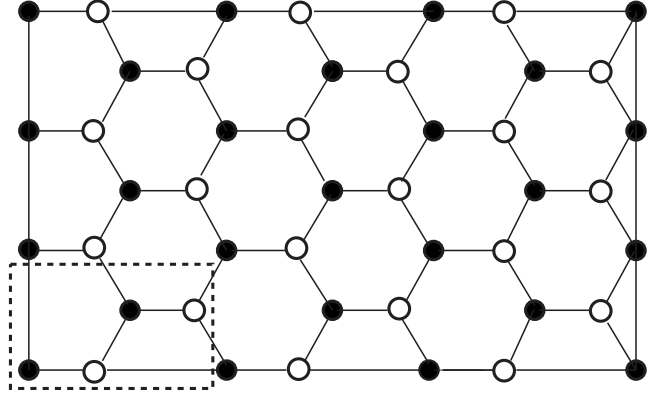


FIG. 1. The periodic honeycomb lattice consisting of two triangular sublattices A and B , which are depicted by solid and open circles, respectively. The dashed rectangle is an elementary cell for building a periodic honeycomb lattice covering a rectangular area.

A physical quantity of central interest is the staggered susceptibility (corresponding to the third component of the staggered magnetization M_s^3), which is given by

$$\begin{aligned} \chi_s &= \frac{1}{L_1 L_2} \int_0^\beta dt \langle M_s^3(0) M_s^3(t) \rangle \\ &= \frac{1}{L_1 L_2} \int_0^\beta dt \frac{1}{Z} \text{Tr} [M_s^3(0) M_s^3(t) \exp(-\beta H)]. \end{aligned} \quad (5)$$

Here β is the inverse temperature, L_1 and L_2 are the spatial box sizes in the x_1 and x_2 directions, respectively, and

$$Z = \text{Tr} \exp(-\beta H) \quad (6)$$

is the partition function. The staggered magnetization order parameter \vec{M}_s is defined by

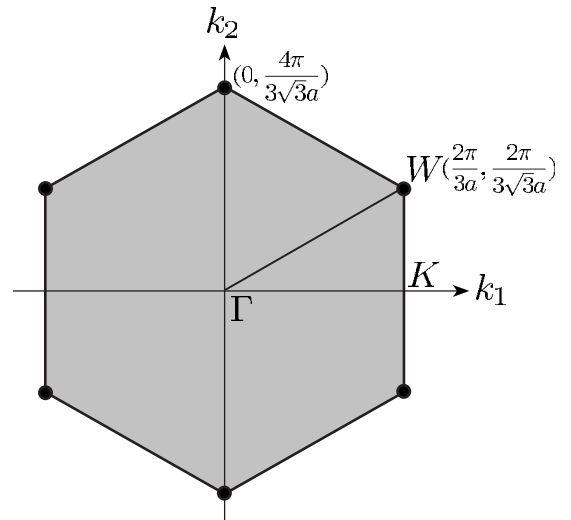


FIG. 2. The momentum space of a honeycomb lattice, which is a doubly covered Brillouin zone dual to the two triangular sublattices A and B .

$$\vec{M}_s = \sum_x (-1)^x \vec{S}_x. \quad (7)$$

Here $(-1)^x=1$ on the A sublattice and $(-1)^x=-1$ on the B sublattice, respectively. Another relevant quantity is the uniform susceptibility which is given by

$$\begin{aligned} \chi_u &= \frac{1}{L_1 L_2} \int_0^\beta dt \langle M^3(0) M^3(t) \rangle \\ &= \frac{1}{L_1 L_2} \int_0^\beta dt \frac{1}{Z} \text{Tr}[M^3(0) M^3(t) \exp(-\beta H)]. \end{aligned} \quad (8)$$

Here

$$\vec{M} = \sum_x \vec{S}_x \quad (9)$$

is the uniform magnetization. Both χ_s and χ_u can be measured very efficiently with the loop-cluster algorithm using improved estimators.¹⁸ In particular, in the multicluster version of the algorithm the staggered susceptibility is given in terms of the cluster sizes $|C|$ (which have the dimension of time), i.e.,

$$\chi_s = \frac{1}{4\beta L^2} \left\langle \sum_c |C|^2 \right\rangle. \quad (10)$$

Similarly, the uniform susceptibility

$$\chi_u = \frac{\beta}{4L^2} \langle W_i^2 \rangle = \frac{\beta}{4L^2} \left\langle \sum_c W_i(C)^2 \right\rangle \quad (11)$$

is given in terms of the temporal winding number $W_i = \sum_c W_i(C)$ which is the sum of winding numbers $W_i(C)$ of the loop clusters C around the Euclidean time direction. Similarly, the spatial winding numbers are defined by $W_i = \sum_c W_i(C)$ with $i \in \{1, 2\}$.

III. LOW-ENERGY EFFECTIVE THEORY FOR MAGNONS

Due to the spontaneous breaking of the $SU(2)_s$ spin symmetry down to its $U(1)_s$ subgroup, the low-energy physics of antiferromagnets is governed by two massless Goldstone bosons, the antiferromagnetic spin waves or magnons. The description of the low-energy magnon physics by an effective theory was pioneered by Chakravarty *et al.* in Ref. 10. In analogy to chiral perturbation theory for the pseudo-Goldstone pions in QCD, a systematic low-energy effective field theory for magnons was developed in Refs. 11–14. The staggered magnetization of an antiferromagnet can be described by a unit-vector field $\vec{e}(x)$ in the coset space $SU(2)_s/U(1)_s=S^2$, i.e.,

$$\vec{e}(x) = [e_1(x), e_2(x), e_3(x)], \quad \vec{e}(x)^2 = 1. \quad (12)$$

Here $x=(x_1, x_2, t)$ denotes a point in $(2+1)$ -dimensional space-time. To leading order, the Euclidean magnon low-energy effective action takes the form

$$S[\vec{e}] = \int d^2x dt \frac{\rho_s}{2} \left(\partial_i \vec{e} \cdot \partial_i \vec{e} + \frac{1}{c^2} \partial_t \vec{e} \cdot \partial_t \vec{e} \right), \quad (13)$$

where the index $i \in \{1, 2\}$ labels the two spatial directions and t refers to the Euclidean time direction. The parameter ρ_s is the spin stiffness and c is the spin-wave velocity. At low energies the antiferromagnet has a relativistic spectrum.

Using the above Euclidean action, detailed calculations of a variety of physical quantities including the next-to-next-to-leading-order contributions have been carried out in Ref. 27. Here we only quote the results that are relevant for our study, namely, the finite-temperature and finite-volume effects of the staggered and uniform susceptibilities, as well as results on the rotor spectrum of the antiferromagnet in a finite volume. The aspect ratio of a spatially quadratic space-time box with $L_1=L_2=L$ is characterized by $l=(\beta c/L)^{1/3}$, with which one distinguishes cubical space-time volumes with $\beta c \approx L$ from cylindrical ones with $\beta c \gg L$. In the cubical regime the volume and temperature dependence of the staggered susceptibility is given by

$$\begin{aligned} \chi_s &= \frac{\mathcal{M}_s^2 L^2 \beta}{3} \left\{ 1 + 2 \frac{c}{\rho_s L l} \beta_1(l) + \left(\frac{c}{\rho_s L l} \right)^2 [\beta_1(l)^2 + 3\beta_2(l)] \right. \\ &\quad \left. + O\left(\frac{1}{L^3}\right) \right\}, \end{aligned} \quad (14)$$

where \mathcal{M}_s is the staggered magnetization density. The uniform susceptibility takes the form

$$\begin{aligned} \chi_u &= \frac{2\rho_s}{3c^2} \left\{ 1 + \frac{1}{3} \frac{c}{\rho_s L l} \tilde{\beta}_1(l) + \frac{1}{3} \left(\frac{c}{\rho_s L l} \right)^2 \right. \\ &\quad \left. \times \left[\tilde{\beta}_2(l) - \frac{1}{3} \tilde{\beta}_1(l)^2 - 6\psi(l) \right] + O\left(\frac{1}{L^3}\right) \right\}. \end{aligned} \quad (15)$$

The functions $\beta_i(l)$, $\tilde{\beta}_i(l)$, and $\psi(l)$, which only depend on l , are shape coefficients of the space-time box defined in Ref. 27. In the very low-temperature limit, one enters the cylindrical regime of space-time volumes with $\beta c \gg L$. In this case, the staggered magnetization vector \vec{M}_s acts as a quantum rotor, and correspondingly, the low-energy end of the spectrum takes the form

$$E_S = \frac{S(S+1)}{2\Theta}. \quad (16)$$

Here $S \in \{0, 1, 2, \dots\}$ is the spin and Θ is the moment of inertia of the quantum rotor which is given by²⁷

$$\Theta = \frac{\rho_s L^2}{c^2} \left[1 + \frac{3.900\,265c}{4\pi\rho_s L} + O\left(\frac{1}{L^2}\right) \right]. \quad (17)$$

The partition function of the $(2S+1)$ -fold degenerate rotor spectrum is given by

$$Z = \sum_{S=0}^{\infty} (2S+1) \exp(-\beta E_S). \quad (18)$$

The probability distribution of the uniform magnetization $M^3=S^3$ is then given by

TABLE I. Some numerical data for the staggered susceptibility χ_s and the temporal winding number squared $\langle W_T^2 \rangle$ obtained with the loop-cluster algorithm. N_1 and N_2 count the number of copies of elementary rectangles in the one and two directions and $N_{\text{spin}}=4N_1N_2$ is the corresponding number of spins.

βJ	N_1	N_2	N_{spin}	$\chi_s J a$	$\langle W_T^2 \rangle$
24	11	19	836	575.14(82)	7.828(15)
25	11	19	836	597.58(85)	7.494(15)
26	11	19	836	620.91(85)	7.177(15)
34	15	26	1560	1450(3)	10.113(20)
35	15	26	1560	1496(3)	9.797(21)
36	15	26	1560	1532(3)	9.491(22)
44	19	33	2508	2936(5)	12.411(25)
45	19	33	2508	3001(5)	12.145(25)
46	19	33	2508	3061(5)	11.848(26)
48	22	38	3344	4220(6)	15.137(28)
49	22	38	3344	4308(7)	14.796(26)
50	22	38	3344	4392(7)	14.495(28)
59	26	45	4680	7151(11)	17.123(29)
60	26	45	4680	7286(11)	16.838(29)
61	26	45	4680	7401(12)	16.557(31)

$$p(M^3) = \frac{1}{Z} \sum_{S \geq |M^3|} \exp(-\beta E_S). \quad (19)$$

IV. DETERMINATION OF THE LOW-ENERGY PARAMETERS OF THE UNDOPED SYSTEM

In order to determine the low-energy constants \mathcal{M}_s , ρ_s , and c , we have performed numerical simulations of the Heisenberg model on the honeycomb lattice with up to 4680 spins in the cubical and cylindrical regimes. The cubical regime is determined by the condition $\langle \sum_C W_1(C)^2 \rangle \approx \langle \sum_C W_2(C)^2 \rangle \approx \langle \sum_C W_T(C)^2 \rangle$ (which implies that $\beta c \approx L$). The chiral perturbation-theory predictions for χ_s and χ_u in Eqs. (14) and (15) are derived for a (2+1)-dimensional box with equal extent in the two spatial directions (which we refer to as a square-shaped area). Since it is not possible to consider the honeycomb geometry on an exactly square-shaped area, our simulations are done on almost square-shaped rectangles. To be more precise, the lattices used in our simulations deviate from a perfect square shape by less than 0.4%. We have performed an interpolation on some of our data to the exactly square-shaped area and find agreement between the fits of the interpolated and the raw data. The inclusion of $O(1/L^3)$ corrections in the fits leads to consistent results as well. Instead of considering the staggered magnetization density \mathcal{M}_s of Eq. (14), we choose to quote the staggered magnetization per spin $\tilde{\mathcal{M}}_s$, which is related to \mathcal{M}_s by

$$\tilde{\mathcal{M}}_s = \frac{3\sqrt{3}}{4} \mathcal{M}_s a^2. \quad (20)$$

Some numerical data from our simulations are listed in Table I. By fitting χ_s and χ_u simultaneously to Eqs. (14) and

(15), we find

$$\tilde{\mathcal{M}}_s = 0.2688(3), \quad \rho_s = 0.102(2)J, \quad c = 1.297(16)Ja \quad (21)$$

with $\chi^2/\text{DOF} \approx 1.05$ (see Figs. 3 and 4). The low-energy constants ρ_s and c are determined with high accuracy (at the percent level). The error of $\tilde{\mathcal{M}}_s$ is even at the permille level. The value of c obtained here is consistent with the one of a spin-wave expansion study.²⁸ The above value of $\tilde{\mathcal{M}}_s$ is larger than the one of a previous spin-wave expansion²⁹ but consistent with that of a series-expansion study³⁰ (within the comparably large 4% error of that study). It is only slightly larger than the value obtained in a previous Monte Carlo

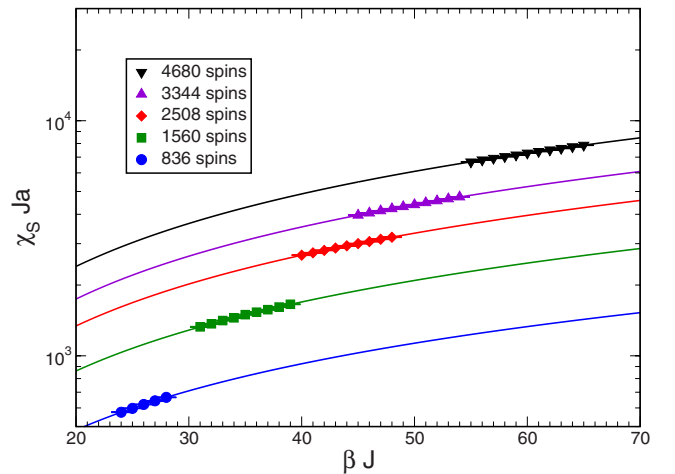


FIG. 3. (Color online) Fit of the finite-size and finite-temperature effects of the staggered susceptibility χ_s to the results of the effective theory in the cubical regime.

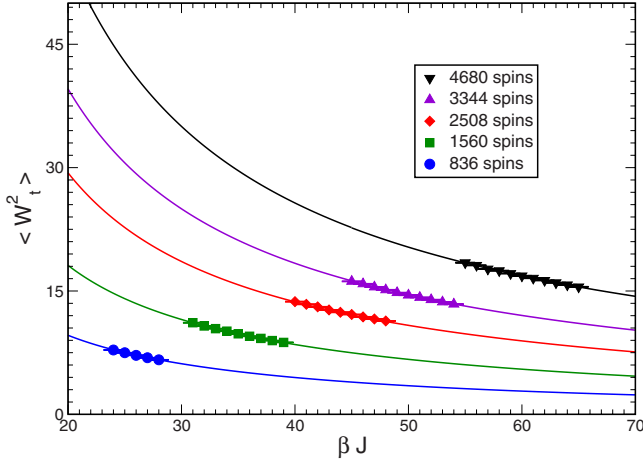


FIG. 4. (Color online) Fit of the finite-size and finite-temperature effects of the temporal winding number squared $\langle W_t^2 \rangle$ to the results of the effective theory in the cubical regime.

calculation $\tilde{\mathcal{M}}_s=0.2677(6)$.²⁵ We want to point out that our results are obtained by fitting more than 80 numerical data points to two analytic predictions with only three unknown parameters. If $\tilde{\mathcal{M}}_s$ is fixed to 0.2677, the quality of our fit downgrades to $\chi^2/\text{DOF} \approx 3.0$. The reduction of $\tilde{\mathcal{M}}_s=0.2688(3)$ and $\rho_s=0.102(2)J$ on the honeycomb lattice compared to those on the square lattice [$\tilde{\mathcal{M}}_s=0.3074(4)$ and $\rho_s=0.186(4)J$ (Refs. 18 and 19)] indicates larger quantum fluctuations on the honeycomb lattice. This is expected since the coordination number of the honeycomb lattice is smaller than the one of the square lattice.

Having determined the values of the low-energy parameters $\tilde{\mathcal{M}}_s$, ρ_s , and c from the cubical space-time volume regime, we can test the effective theory in the cylindrical regime. Figure 5 shows a comparison of the effective theory prediction for the probability distribution $p(M^3)$ of Eq. (19) with Monte Carlo data. The observed excellent agreement—which does not involve any adjustable parameters—confirms

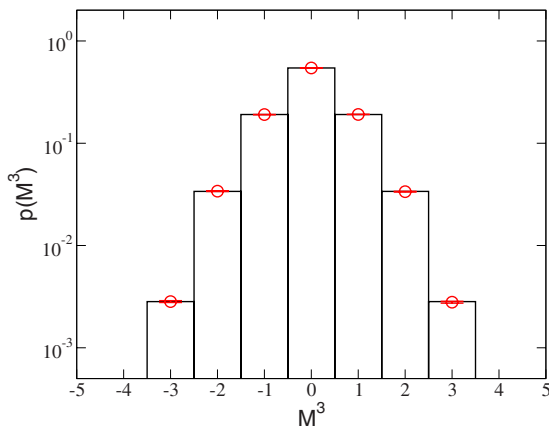


FIG. 5. (Color online) Comparison of the effective theory prediction for the probability distribution $p(M^3)$ of Eq. (19) with Monte Carlo data on an $N_1 \times N_2 = 11 \times 19$ honeycomb lattice with $N_{\text{spin}}=836$ at $\beta J=60$. The open circles are the Monte Carlo data while the histogram is the effective theory prediction.

the quantitative correctness of the effective theory.

V. SINGLE-HOLE DISPERSION RELATION

The physics of a single hole on the honeycomb lattice was studied theoretically in Ref. 26 using exact diagonalization, series expansion, and self-consistent Born approximation. Here we use first-principles Monte Carlo simulations to quantitatively investigate the single-hole dispersion relation and quasiparticle weight. To achieve this goal, we have implemented a technique similar to the one used in Ref. 5 to simulate the one-hole sector of the t - J model. Some details of the numerical method are described in the Appendix. When one calculates the fermion two-point function in momentum space, one should keep in mind that the Brillouin zone of the honeycomb lattice is doubly covered. The two covers are dual to the two triangular Bravais sublattices A and B . Therefore, one needs to distinguish the correlators between AA , AB , BA , and BB sublattices. The correlation function between AA sublattices with momentum k takes the form

$$G^{AA}(k, t) = \frac{1}{Z} \sum_{x, y \in A} \text{Tr}[c_x^\dagger(0)c_y(t)\exp(-\beta H)]\exp[-ik(x-y)] \sim \sum_{n=1}^{\infty} Z_n(k)\exp\{-[E_n(k) - E_0]t\}, \quad (22)$$

where E_0 is the ground-state energy of the half-filled system and

$$Z_n(k) = \left| \langle 0 | \sum_{x \in A} c_x \exp(ikx) | n \rangle \right|^2. \quad (23)$$

The factor $Z_1(k)$ is known as the quasiparticle weight. In deriving Eq. (22), we have inserted a complete set of energy eigenstates $1 = \sum_n |n\rangle\langle n|$ in the single-hole sector and taken the limit $\beta \rightarrow \infty$ in the final step. The fermion energy

$$E_h(k) = E_1(k) - E_0 \quad (24)$$

corresponding to the momentum k can be extracted by fitting the data to a single or a double exponential. The correlation function between AA sublattices with momentum $k = (\frac{2\pi}{3a}, \frac{2\pi}{3\sqrt{3}a})$ depicted in Fig. 6 is obtained on a honeycomb lattice with 3456 spins at $J/t=2.0$. A single-exponential fit yields $E_h(k)=0.207(9)t$, while a double-exponential fit gives the consistent result $E_h(k)=0.201(5)t$. In the same way, we have determined the one-hole dispersion relation from the AA correlator for all momenta k . The single-hole dispersion relation in Fig. 7 is obtained with the same parameters as in Fig. 6. Each energy $E_h(k)$ in Fig. 7 is obtained directly from the corresponding correlation function. We have performed the same analysis on a smaller lattice, and we find that the dispersion relation as well as the physical quantities derived from it do not suffer from finite-size effects. The figure shows that the hole pockets are located at $(\pm \frac{2\pi}{3a}, \pm \frac{2\pi}{3\sqrt{3}a})$ and $(0, \pm \frac{4\pi}{3\sqrt{3}a})$ in the Brillouin zone. The position of the hole pockets agrees with the position of the Dirac cones obtained from the free fermion theory on the honeycomb lattice which is relevant for graphene.

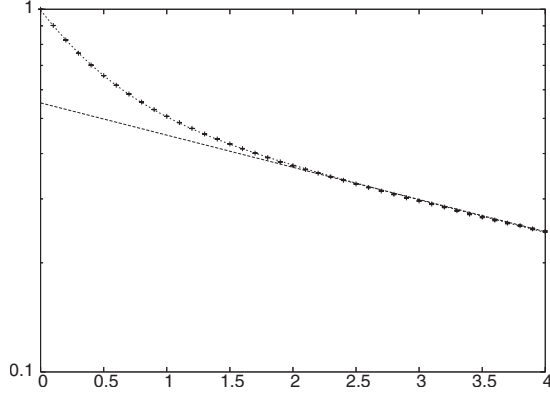


FIG. 6. Correlation function $G^{AA}(k, t)$ between AA sublattices with Fourier momentum $k = (\frac{2\pi}{3a}, \frac{2\pi}{3\sqrt{3}a})$. The lower line is the result of a single-exponential fit, while the upper curve is obtained from a double-exponential fit.

VI. EFFECTIVE FIELD THEORY FOR HOLES AND MAGNONS

Motivated by baryon chiral perturbation theory for QCD,^{31–35} based on symmetry considerations a universal effective theory for magnons and charge carriers in lightly doped antiferromagnets on the square lattice has been constructed using the known location of hole or electron pockets. This powerful method was used to systematically construct the effective theory for t - J -type models on the square lattice in Refs. 15, 16, and 36. The effective theories were used to investigate the one-magnon exchange potential and the resulting bound states between two holes and two electrons as well as the possible existence of spiral phases.^{16,36,37} Using the information about the location of the pockets, based on the symmetry properties of the underlying microscopic theory, we have constructed a systematic low-energy effective theory for the t - J model on the honeycomb lattice. The details of the construction of the effective theory will be described in a forthcoming publication. Here we briefly sketch the principles behind this construction and present the terms in the effective Lagrangian that are relevant for our present study. In the effective theory, the holes which reside in momentum space pockets centered at

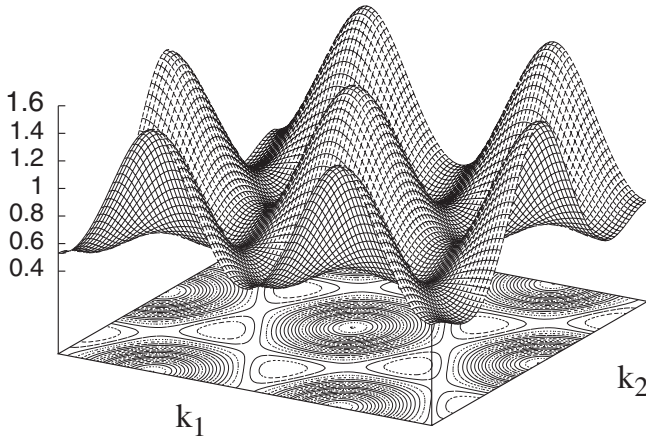


FIG. 7. The dispersion relation $E_h(k)/t$ for a single hole in an antiferromagnet on the honeycomb lattice.

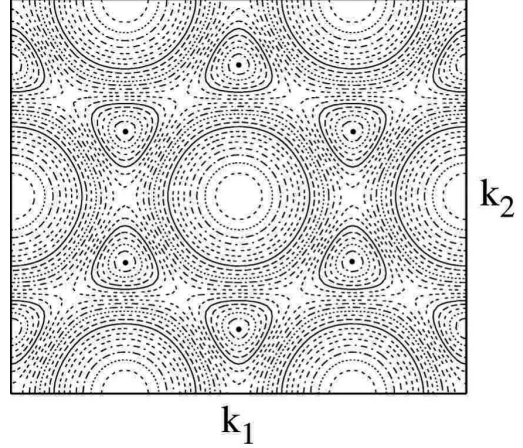


FIG. 8. Circular hole pockets on the honeycomb lattice. The dots mark the centers of the hole pockets (corresponding to the point W and its symmetry partners). The parameters are the same as in Fig. 7.

$$k^\alpha = \left(0, \frac{4\pi}{3\sqrt{3}a}\right), \quad k^\beta = \left(0, -\frac{4\pi}{3\sqrt{3}a}\right) \quad (25)$$

are represented by Grassmann fields $\psi_s^f(x)$. Here the “flavor” index $f = \alpha, \beta$ characterizes the corresponding hole pocket and the index $s = \pm$ denotes spin parallel (+) or antiparallel (–) to the local staggered magnetization. The magnons are coupled to the holes through a nonlinear realization of the spontaneously broken $SU(2)_s$ symmetry. The global $SU(2)_s$ symmetry then manifests itself as a local $U(1)_s$ symmetry in the unbroken subgroup. This construction leads to an Abelian “gauge” field $v_\mu^3(x)$ and to two vector fields $v_\mu^\pm(x)$ which are “charged” under $U(1)_s$ spin transformations. The coupling of magnons and holes is realized through $v_\mu^3(x)$ and $v_\mu^\pm(x)$. These fields have a well-defined transformation behavior under the symmetries which the effective theory inherits from the underlying microscopic models. Based on symmetry considerations, we have constructed the leading-order terms of the effective Lagrangian for magnons and holes on the honeycomb lattice. In this paper we only list those terms that are relevant for the propagation of a single hole, i.e.,

$$\mathcal{L} = \sum_{\substack{f=\alpha,\beta \\ s=+,-}} \left[M \psi_s^{f\dagger} \psi_s^f + \psi_s^{f\dagger} D_t \psi_s^f + \frac{1}{2M'} D_i \psi_s^{f\dagger} D_i \psi_s^f \right]. \quad (26)$$

Here M is the rest mass and M' is the kinetic mass of a hole, while D_μ is a covariant derivative given by

$$D_\mu \psi_\pm^f(x) = [\partial_\mu \pm i v_\mu^3(x)] \psi_\pm^f(x). \quad (27)$$

Equation (26) yields circular hole pockets for small momenta which is indeed confirmed in Fig. 8. As illustrated in Fig. 9, the low-energy constant M' in Eq. (26) is obtained from the curvature of the dispersion $E_h(k)$ near a minimum. While Fig. 9 just shows a one-dimensional cut through the center of a hole pocket, the fit actually involves points from a two-dimensional region in momentum space. The two fit parameters are the rest mass M and the kinetic mass M' . Properly

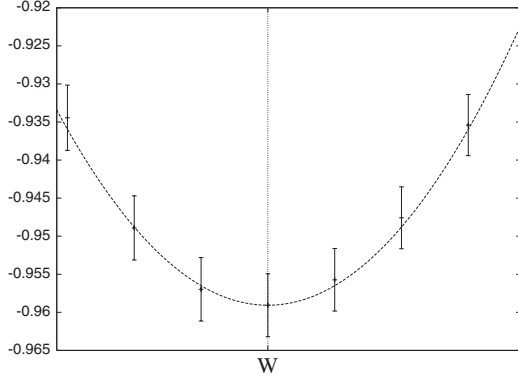


FIG. 9. Fit of the kinetic mass M' to the dispersion relation $E_h(k)$ near the center of a hole pocket.

taking into account the correlation of the error bars, one obtains good fits. For example, on a honeycomb lattice with 3456 spins and $J/t=2.0$, we find $M'ta^2=4.1(1)$.

In Figs. 10 and 11, we have plotted the single-hole dispersion as well as the quasiparticle residue $Z_1(k)$ over the irreducible wedge Γ - K - W - Γ of the Brillouin zone for $J/t=1.0$. The resulting bandwidth

$$\Delta = E_h(\Gamma) - E_h(W) \quad (28)$$

is in qualitative agreement with exact diagonalization and series-expansion results obtained in Ref. 26. While exact diagonalization of small systems may suffer from finite-size effects, and series expansions may not converge in all regions of parameter space, the Monte Carlo data obtained with the efficient loop-cluster algorithm do not suffer from systematic uncertainties. In Table II we list the kinetic mass M' as well as the bandwidth Δ for a few values of J/t .

VII. CONCLUSIONS

We have studied antiferromagnetism on the honeycomb lattice by first-principles Monte Carlo calculations. In particular, we have fitted more than hundred Monte Carlo data obtained at rather different volumes and temperatures with just four low-energy parameters— \mathcal{M}_s , ρ_s , c , and M' —of the

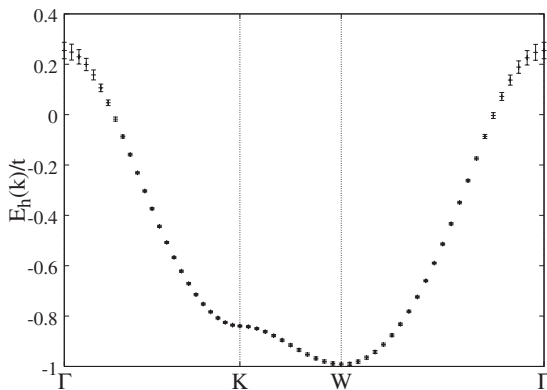


FIG. 10. Dispersion relation $E_h(k)/t$ of a single hole for $J/t=1.0$ along the irreducible wedge Γ - K - W - Γ in the first Brillouin zone (see Fig. 2).

TABLE II. Kinetic mass M' as well as the bandwidth Δ for some values of J/t .

J/t	$M'ta^2$	Δ/t
2.0	4.1(1)	1.15(3)
1.5	2.9(1)	1.25(3)
1.0	1.9(1)	1.24(4)
0.9	1.8(1)	1.15(6)
0.6	1.5(2)	0.9(1)

effective theory for the t - J model. These parameters have been determined with percent and sometimes even with per mille accuracy. This should demonstrate convincingly that the systematic low-energy effective field theory yields quantitatively correct results for the physics of magnons and holes. Hence, the effective theory allows us to perform unbiased investigations of the low-energy physics of the system. The construction of the effective theory for lightly doped antiferromagnets, as well as a systematic investigation of the one-magnon exchange potential and the resulting bound states between two holes, as well as the possible existence of spiral phases of lightly doped antiferromagnets on the honeycomb lattice will be presented in subsequent studies.

ACKNOWLEDGMENTS

We would like to thank M. Pepe for his collaboration on a related problem for which he developed the reweighting technique used to evaluate the fermionic two-point function. We have benefited from discussions with P. Hasenfratz and F. Niedermayer. We also thank C. Bolliger and O. P. Sushkov for helpful correspondence. This work was supported in parts by the Schweizerischer Nationalfonds. The ‘‘Center for Research and Education in Fundamental Physics’’ at Bern University is supported by the ‘‘Innovations- und Kooperationsprojekt C-13’’ of the Schweizerische Universitätskonferenz (SUK/CRUS).

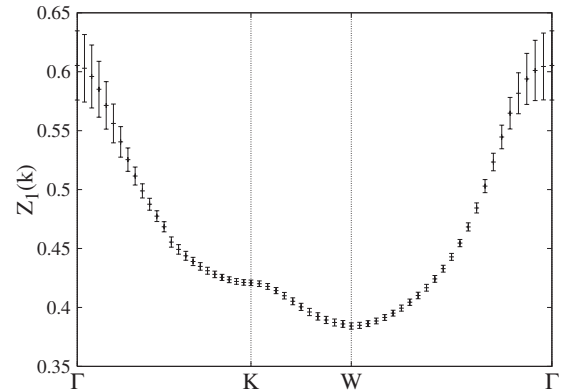
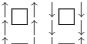
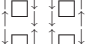





FIG. 11. The quasiparticle weight $Z_1(k)$ of a single hole for $J/t=1.0$ along the irreducible wedge Γ - K - W - Γ in the first Brillouin zone (see Fig. 2).

TABLE III. Space-time plaquette configurations for a nearest-neighbor pair of sites and their corresponding Boltzmann weights. The diamond \diamond stands for a hole, while \uparrow and \downarrow represent a fermion with spins up and down, respectively.

Plaquettes	Weights
	$\exp(-\epsilon J/4)$
	$\exp(\epsilon J/4)\cosh(\epsilon J/2)$
	$-\exp(\epsilon J/4)\sinh(\epsilon J/2)$
	$\cosh(\epsilon t)$
	$\sinh(\epsilon t)$

APPENDIX: THE FERMION TWO-POINT CORRELATION FUNCTION

In this appendix, we explain the algorithm used to calculate the fermion correlation function, which is similar to the one used in Ref. 5. An alternative efficient method is the one described in Ref. 6. In coordinate space, the fermion two-point correlation function is given by

$$G(x-y, \tau) = \frac{1}{Z} \text{Tr}_{Q=0} \{ c_x^\dagger \exp(-\tau H) c_y \exp[-(\beta-\tau)H] \}. \quad (\text{A1})$$

Here the charge Q represents fermion number relative to half filling, and $\text{Tr}_{Q=0}$ sums over all states of the half-filled system. In particular,

$$Z = \text{Tr}_{Q=0} [\exp(-\beta H)] \quad (\text{A2})$$

is the partition function in the zero-hole sector (i.e., the one of the Heisenberg model). By introducing a Trotter decomposition of the Hamiltonian and by inserting complete sets of states between discrete Euclidean time steps, one arrives at a path-integral representation of the fermion two-point function. The configurations contributing to the path integral contain a single hole propagating between the time slices at $t=0$ and τ , in which the hole is created and annihilated. The other time slices are half filled and thus represent states of the Heisenberg model. The Boltzmann weight of a configuration is a product of contributions associated with space-time plaquettes corresponding to a pair of nearest-neighbor sites propagating by one discrete time step. The allowed plaquette configurations and their corresponding Boltzmann weights are listed in Table III.

The numerical method is based on the loop-cluster algorithm for the Heisenberg model, which is used to generate half-filled configurations without holes, based on importance sampling using the Euclidean action of the Heisenberg model. A fermion configuration that contributes to the two-

point function contains a hole created at the site x at time $t=0$ and annihilated later at $t=\tau$ at the site y . To each fermion configuration of this kind, one can uniquely associate a half-filled Heisenberg model configuration simply by replacing the hole with a spin up or down, depending on which type of hole was propagating. The contribution of a fermion path to the two-point function is obtained by reweighting it with the ratio of its own Boltzmann factor and the Boltzmann factor associated with the corresponding half-filled Heisenberg model configuration which was used for importance sampling. Since each Boltzmann factor is a product of local plaquette contributions, and since the hole configuration and the corresponding Heisenberg model configuration differ only along the hole path, the ratio of the two Boltzmann factors is a product of space-time plaquette ratios along the path of the hole.

It is important to note that many hole configurations are associated with the same half-filled Heisenberg model configuration. The reweighting method sums the contributions of all those hole configurations to the two-point function. A single hole is propagated through the background of each Heisenberg model configuration generated by the loop algorithm using the following method. Starting from the site x at which the hole is created at time $t=0$, the hole is propagated forward, step by step in Euclidean time. In the first discrete time step, the hole may stay at the initial site x or may hop to a neighboring site, provided that an allowed configuration (with nonzero Boltzmann weight) is generated on the corresponding space-time plaquette when one replaces a spin by the hole. In particular, when the hole enters a plaquette on which all four spins are parallel, it can either stay where it is or hop to the neighboring site. On the other hand, when the hole enters a plaquette with antiparallel spins, it must follow the path of the corresponding spin. The weight of a hole path reaching a point in the next time slice results from the ratio of the Boltzmann factors of the new spin-hole space-time plaquette configuration and the original pure spin Heisenberg model configuration. The propagation to the next time slices then proceeds iteratively, always using the propagator already built for the previous time slice. In this way, further ratios of spin-hole plaquette weights and original pure spin plaquette weights enter as multiplicative factors in the two-point function. At the end of this procedure the two-point function has been calculated for all sites y in all time slices through which one has propagated the hole.

It should be noted that this method suffers from a sign problem because one of the Boltzmann weights in Table III is negative. Fortunately, this sign problem is mild in large regions of parameter space. Although the method can also be implemented in continuous time, in this paper we work in discrete time, always quoting results in the time-continuum limit.

*fjjiang@itp.unibe.ch

†fkampfer@itp.unibe.ch

‡nyfeler@itp.unibe.ch

§wiese@itp.unibe.ch

- ¹G. J. Bednorz and K. A. Müller, *Z. Phys. B: Condens. Matter* **64**, 189 (1986).
- ²R. Eder, Y. Ohta, and G. A. Sawatzky, *Phys. Rev. B* **55**, R3414 (1997).
- ³T. K. Lee and C. T. Shih, *Phys. Rev. B* **55**, 5983 (1997).
- ⁴C. J. Hamer, Z. Weihong, and J. Oitmaa, *Phys. Rev. B* **58**, 15508 (1998).
- ⁵M. Brunner, F. F. Assaad, and A. Muramatsu, *Phys. Rev. B* **62**, 15480 (2000).
- ⁶A. S. Mishchenko, N. V. Prokof'ev, and B. V. Svistunov, *Phys. Rev. B* **64**, 033101 (2001).
- ⁷B. O. Wells, Z. X. Shen, A. Matsuura, D. M. King, M. A. Kastner, M. Greven, and R. J. Birgeneau, *Phys. Rev. Lett.* **74**, 964 (1995).
- ⁸S. La Rosa, I. Vobornik, F. Zwick, H. Berger, M. Grioni, G. Margaritondo, R. J. Kelley, M. Onellion, and A. Chubukov, *Phys. Rev. B* **56**, R525 (1997).
- ⁹C. Kim, P. J. White, Z.-X. Shen, T. Tohyama, Y. Shibata, S. Maekawa, B. O. Wells, Y. J. Kim, R. J. Birgeneau, and M. A. Kastner, *Phys. Rev. Lett.* **80**, 4245 (1998).
- ¹⁰S. Chakravarty, B. I. Halperin, and D. R. Nelson, *Phys. Rev. B* **39**, 2344 (1989).
- ¹¹H. Neuberger and T. Ziman, *Phys. Rev. B* **39**, 2608 (1989).
- ¹²D. S. Fisher, *Phys. Rev. B* **39**, 11783 (1989).
- ¹³P. Hasenfratz and H. Leutwyler, *Nucl. Phys. B* **343**, 241 (1990).
- ¹⁴P. Hasenfratz and F. Niedermayer, *Phys. Lett. B* **268**, 231 (1991).
- ¹⁵F. Kämpfer, M. Moser, and U.-J. Wiese, *Nucl. Phys. B* **729**, 317 (2005).
- ¹⁶C. Brügger, F. Kämpfer, M. Moser, M. Pepe, and U.-J. Wiese, *Phys. Rev. B* **74**, 224432 (2006).
- ¹⁷H. G. Evertz, G. Lana, and M. Marcu, *Phys. Rev. Lett.* **70**, 875 (1993).
- ¹⁸U.-J. Wiese and H.-P. Ying, *Z. Phys. B: Condens. Matter* **93**, 147 (1994).
- ¹⁹B. B. Beard and U.-J. Wiese, *Phys. Rev. Lett.* **77**, 5130 (1996).
- ²⁰O. I. Motrunich and P. A. Lee, *Phys. Rev. B* **69**, 214516 (2004).
- ²¹W. Zheng, J. Oitmaa, C. J. Hamer, and R. R. P. Singh, *Phys. Rev. B* **70**, 020504(R) (2004).
- ²²H. Watanabe and M. Ogata, *J. Phys. Soc. Jpn.* **74**, 2901 (2005).
- ²³A. H. Castro Neto, F. Guinea, N. M. R. Peres, K. S. Novoselov, and A. K. Geim, arXiv:0709.1163, *Rev. Mod. Phys.* (to be published).
- ²⁴I. F. Herbut, *Phys. Rev. Lett.* **97**, 146401 (2006).
- ²⁵E. V. Castro, N. M. R. Peres, K. S. D. Beach, and A. W. Sandvik, *Phys. Rev. B* **73**, 054422 (2006).
- ²⁶A. Lüscher, A. Läuchli, W. Zheng, and O. P. Sushkov, *Phys. Rev. B* **73**, 155118 (2006).
- ²⁷P. Hasenfratz and F. Niedermayer, *Z. Phys. B: Condens. Matter* **92**, 91 (1993).
- ²⁸A. Mattsson, P. Fröjdh, and T. Einarsson, *Phys. Rev. B* **49**, 3997 (1994).
- ²⁹Zheng Weihong, J. Oitmaa, and C. J. Hamer, *Phys. Rev. B* **44**, 11869 (1991).
- ³⁰J. Oitmaa, C. J. Hamer, and Zheng Weihong, *Phys. Rev. B* **45**, 9834 (1992).
- ³¹H. Georgi, *Weak Interactions and Modern Particle Theory* (Benjamin, New York, 1984).
- ³²J. Gasser, M. E. Sainio, and A. Svarc, *Nucl. Phys. B* **307**, 779 (1988).
- ³³E. Jenkins and A. Manohar, *Phys. Lett. B* **255**, 558 (1991).
- ³⁴V. Bernard, N. Kaiser, J. Kambor, and U.-G. Meissner, *Nucl. Phys. B* **388**, 315 (1992).
- ³⁵T. Becher and H. Leutwyler, *Eur. Phys. J. C* **9**, 643 (1999).
- ³⁶C. Brügger, C. P. Hofmann, F. Kämpfer, M. Moser, M. Pepe, and U.-J. Wiese, *Phys. Rev. B* **75**, 214405 (2007).
- ³⁷C. Brügger, C. P. Hofmann, F. Kämpfer, M. Pepe, and U.-J. Wiese, *Phys. Rev. B* **75**, 014421 (2007).